

Effect of Grain Size on Differential Desorption of Volatile Species and on Non-ideal MHD Diffusivity

Bo Zhao¹★†, Paola Caselli¹, Zhi-Yun Li²

¹Max-Planck-Institut für extraterrestrische Physik (MPE), Garching, Germany, 85748

²University of Virginia, Astronomy Department, Charlottesville, USA, 22904

25 May 2022

ABSTRACT

We developed a chemical network for modeling the chemistry and non-ideal MHD effects from the collapsing dense molecular clouds to protostellar disks. First, we re-formulated the cosmic-ray desorption rate by considering the variations of desorption rate over the grain size distribution. We find that the differential desorption of volatile species is amplified by the grains larger than $0.1 \mu\text{m}$, because larger grains are heated to a lower temperature by cosmic-rays and hence more sensitive to the variations in binding energies. As a result, atomic nitrogen N is ~ 2 orders of magnitude more abundant than CO; N_2H^+ also becomes a few times more abundant than HCO^+ due to the increased gas-phase N_2 . However, the changes in ionization fraction due to freeze-out and desorption only have minor effects on the non-ideal MHD diffusivities. Our chemical network confirms that the very small grains (VSGs: below a few 100 \AA) weakens the efficiency of both ambipolar diffusion and Hall effect. In collapsing dense cores, a maximum ambipolar diffusion is achieved when truncating the MRN size distribution at $0.1 \mu\text{m}$, and for a maximum Hall effect, the truncation occurs at $0.04 \mu\text{m}$. We conclude that the grain size distribution is crucial to the differential depletion between CO and N_2 related molecules, as well as to the non-ideal MHD diffusivities in dense cores.

Key words: interstellar dust grain, astrochemistry, cosmic rays, magnetohydrodynamics

1 INTRODUCTION

In dense molecular cloud cores that are slightly ionized (Bergin & Tafalla 2007), magnetic fields are expected to partially decouple from neutral matter through non-ideal MHD effects, including ambipolar diffusion (AD), Ohmic dissipation, and Hall effect (e.g. Nakano et al. 2002). The non-ideal MHD effects are essentially determined by chemistry and microscopic physical processes (Oppenheimer & Dalgarno 1974; Umebayashi & Nakano 1990). In this way, chemistry actually has a significant impact on the dynamics and evolution of the system, from the collapsing cloud to the planet forming disk. However, until recently, chemistry models in this context are mostly simplified, with little attention paid to how different chemical effects affect the level of non-ideal MHD self-consistently.

When solving the chemical network for non-ideal MHD effects, existing literature often considers a simplified chemical network and treats different molecular and ionic species collectively (e.g., Umebayashi & Nakano 1990; Nishi et al. 1991; Kunz & Mouschovias 2009; Marchand et al. 2016; Wurster 2016; Zhao et al. 2016). In these chemical networks, heavy ions are denoted collectively as m^+

and molecules collectively as m , where m^+ and m are usually assumed to be HCO^+ and CO, respectively. Recently, Dzyurkevich et al. (2017) has developed a more complete chemical network (H-C-O chemistry) for non-ideal MHD effects, yet the effect of grain size on the Hall diffusivity is not fully revealed. Hall effect can dominate over ambipolar diffusion when including grains of ~ 10 – 20 nanometer size, but the values of both diffusivities are not necessarily large enough to allow disk formation. Indeed, there exists an optimal grain size ($a_{\text{min}} \approx 0.04 \mu\text{m}$) to achieve the strongest Hall effect, which we will clarify in this work.

In cold dense cores of molecular clouds, the majority of molecules are frozen onto grain surfaces. The large CO freeze-out implies that HCO^+ will no longer be the main positive charge carrier in dynamically evolved starless cores (i.e., prestellar cores), but H_3^+ and its deuterated isotopologues instead (Caselli et al. 2003; Flower et al. 2005; Tassis et al. 2012). Such a change in ion composition in dense cores has not been considered self-consistently in previous networks for non-ideal MHD diffusivities (Kunz & Mouschovias 2009; Marchand et al. 2016; Wurster 2016; Zhao et al. 2016; Dzyurkevich et al. 2017). We will show that the freeze-out of molecules has limited effect on the non-ideal MHD diffusivities, because the fluid conductivities are dominated by small grains instead of molecular ions; however, it can affect somewhat the polar-

★ Contact e-mail: bo.zhao@mpe.mpg.de

† Present address: Giessenbachstr. 1, D-85748, Garching, Germany

ity and strength of the Hall effect in the intermediate density range $10^9\text{--}10^{11}\text{ cm}^{-3}$ for certain choices of grain size.

Another unsolved puzzle in astrochemistry is the survival of nitrogen bearing species in the gas phase to higher densities than those at which most carbon bearing species are already depleted out (Tafalla et al. 2004; Belloche & André 2004; Bergin et al. 2002). While the difference in binding energies of CO and N₂ is only about 10% (Bergin & Langer 1997; Öberg et al. 2005) and hence is not considered as the origin of the differential depletion between nitrogen and carbon bearing species, it is believed that the loss of gaseous CO may account for the increase in abundances of N₂H⁺ (Aikawa et al. 2001; Bergin et al. 2002; Jørgensen et al. 2004) and thus NH₃ (Geppert et al. 2004; Aikawa et al. 2005). However, it is still a second-order effect compared to the direct freeze-out of neutrals (Bergin & Tafalla 2007). Alternatively, reducing the sticking coefficients of N₂ onto the grains by one order of magnitude can also enhance the abundances of both NH₃ and N₂H⁺ (Flower et al. 2005), yet the approach is somewhat ad hoc. In this work, we present a new way of enhancing the gas-phase abundances of N, N₂ and N₂H⁺ by including the grains size distribution into the formulation of cosmic ray desorption rate. However, due to the large binding energy for NH₃ adopted in this work, it is still difficult to maintain a large amount of gas-phase NH₃ that are efficiently formed via the usual gas-phase route from N₂ (Caselli et al. 2017). More accurate measurements on the binding energies of molecules, as well as the inclusion of surface chemistry are required to better resolve these puzzles.

The rest of the paper is organized as follows. Section 2 describes the set up of the chemical network and the modeling of reaction rates. In Section 3, we show the effect of grain size distribution on the differential desorption of volatile species, followed by a more complete discussion of the effect of grain size on non-ideal MHD diffusivities. Finally, we summarize our main result in Section 4.

2 CHEMICAL NETWORK

We developed a reduced chemical network (Table 1) including the 21 major neutral species in dense molecular cloud, 31 corresponding ion species, electron, and neutral and singly charged grain species. We consider over 500 reactions including gas phase reactions, recombination of charged species on grains, as well as freeze-out onto and thermal desorption of molecules off grains. In contrast to some existing networks (e.g., Garrod et al. 2008), we include all possible charge transfer reactions involving grains (for each size bin; hence the total number of reactions depends on the number of bins), which are crucial for obtaining correct ion abundances in the high density regimes where grains are the dominant charge carriers.

We use the standard grain size distribution $n(a) \propto a^{-\text{Ind}}$ with a fixed power law index *Ind* between the minimum size a_{min} and maximum size a_{max} . The entire size range is divided logarithmically into 20 size bins. The total grain mass is fixed at $q = 1\%$ of the gas mass. The density of grain material is set as $\rho_g = 3.0\text{ g cm}^{-3}$.

2.1 Reactions

The primary mission of a chemical network is to determine the abundance of each species at any given time by solving the coupled rate equations. The rate equation for each species *i* of number density n_i can be expressed by the difference in its formation and

Table 1. Chemical Species

Neutral Species
H ₂ , H, He, C, CH, CH ₂ , CH ₃ , CH ₄ , N, N ₂ , NH, NH ₂ , NH ₃ , O, O ₂ , OH, H ₂ O, CO, CO ₂ , Mg, Fe
Ion Species
H ⁺ , H ₂ ⁺ , H ₃ ⁺ , He ⁺ , HeH ⁺ , C ⁺ , CH ⁺ , CH ₂ ⁺ , CH ₃ ⁺ , CH ₄ ⁺ , CH ₅ ⁺ , N ⁺ , N ₂ ⁺ , N ₂ H ⁺ , NH ⁺ , NH ₂ ⁺ , NH ₃ ⁺ , NH ₄ ⁺ , O ⁺ , O ₂ ⁺ , O ₂ H ⁺ , OH ⁺ , H ₂ O ⁺ , H ₃ O ⁺ , CO ⁺ , HCO ⁺ , CO ₂ ⁺ , HCO ₂ ⁺ , NO ⁺ , Mg ⁺ , Fe ⁺
Electron & Grain Species
e ⁻ , g ⁻ , g ⁺ , g ⁰

destruction:

$$\frac{dn_i}{dt} = \sum_{j,k} k_{jk} n_j n_k + \sum_l k_l n_l - n_i \sum_m k_{im} n_m + (k_{\text{des}} + k_{\text{crd}} + k_{\text{crd,fl}}) n_{i,s} - k_{\text{acc}} n_i, \quad (1)$$

where we include formation of species *i* by two-body reactions (k_{jk}) and cosmic-ray ionization (k_l), and destruction of species *i* by two-body reactions (k_{im}), freeze-out onto dust grains (k_{acc}), thermal (k_{des}) and cosmic-ray desorption from dust grains (k_{crd}), as well as desorption by cosmic-ray induced secondary UV photons ($k_{\text{crd,fl}}$).

The gas-phase reaction rates are taken from UMIST database (McElroy et al. 2013; see also Tomida et al. 2013 and Marchand et al. 2016), formulated by the Arrhenius representation,

$$k(T) = \alpha \left(\frac{T}{300\text{ K}} \right)^\beta \exp\left(-\frac{\gamma}{T}\right), \quad (2)$$

where α is the pre-exponential factor, β characterizes the temperature dependence of the rate coefficient, and γ is the activation energy or energy barrier of the reaction in units of degrees K.

We consider only singly charged grains, which is appropriate for the grain charge population in dense cores (Draine & Sutin 1987; Ivlev et al. 2015b). The reaction rates between gas-phase species and grains are given by (Kunz & Mouschovias 2009),

$$\alpha_{e-g^0} = \pi a^2 \left(\frac{8k_B T}{\pi m_e} \right)^{1/2} \left[1 + \left(\frac{\pi e^2}{2ak_B T} \right)^{1/2} \right] \mathcal{P}_e, \quad (3)$$

$$\alpha_{ig^0} = \pi a^2 \left(\frac{8k_B T}{\pi m_i} \right)^{1/2} \left[1 + \left(\frac{\pi e^2}{2ak_B T} \right)^{1/2} \right] \mathcal{P}_i, \quad (4)$$

$$\alpha_{e-g^+} = \pi a^2 \left(\frac{8k_B T}{\pi m_e} \right)^{1/2} \left[1 + \left(\frac{e^2}{ak_B T} \right) \right] \times \left[1 + \left(\frac{2}{2 + (ak_B T/e^2)} \right)^{1/2} \right] \mathcal{P}_e, \quad (5)$$

$$\alpha_{ig^-} = \pi a^2 \left(\frac{8k_B T}{\pi m_i} \right)^{1/2} \left[1 + \left(\frac{e^2}{ak_B T} \right) \right] \times \left[1 + \left(\frac{2}{2 + (ak_B T/e^2)} \right)^{1/2} \right] \mathcal{P}_i; \quad (6)$$

where k_B is the Boltzmann constant, m_i and m_e are the ion and

electron mass, respectively, and \mathcal{P}_i and \mathcal{P}_e are the sticking probabilities of ions or electrons onto grains, whose values are assigned as 1.0 and 0.6, respectively (Umebayashi 1983; Kunz & Mouschovias 2009).

The rate coefficients for charge transfer between charged grains are given by,

$$\alpha_{g^-g^+} = \pi a_{\text{sum}}^2 \left(\frac{8k_B T}{\pi m_{\text{red}}} \right)^{1/2} \left[1 + \left(\frac{e^2}{a_{\text{sum}} k_B T} \right) \right] \times \left[1 + \left(\frac{2}{2 + (a_{\text{sum}} k_B T / e^2)} \right)^{1/2} \right], \quad (7)$$

where a_{sum} is the sum of the radii of two grains, and $m_{\text{red}} (= m_{g^+} m_{g^-} / (m_{g^+} + m_{g^-}))$ is the reduced mass of the two grains.

The accretion rate of each species onto dust grains is given by,

$$k_{\text{acc}} = \pi a^2 \left(\frac{8k_B T}{\pi m_i} \right)^{1/2} n_g(a), \quad (8)$$

where $n_g(a)$ is the total number density of dust grains with size a .

The thermal desorption rate of species i is given by

$$k_{\text{des}} = v_0(i) \exp \left(\frac{-E_{\text{des}}(i)}{k_B T_d} \right), \quad (9)$$

where T_d is the dust grain temperature that is set to the gas temperature for our application, and $v_0(i)$ is the characteristic vibration frequency for the absorbed species i , given by the following relation,

$$v_0(i) = \sqrt{\frac{2n_s E_{\text{des}}(i)}{\pi^2 m_i}}, \quad (10)$$

where $n_s = 1.5 \times 10^{15} \text{ cm}^{-2}$ is the number of surface sites per cm^2 on grains.

The cosmic-ray particles of few 10^1 to few 10^2 MeV per nucleon can impulsively heat dust grains to a higher temperature T_e (depending on the cosmic ray energy and grain size). The grain subsequently cools through desorption of volatile species, e.g., CO. The rate of such cosmic-ray induced desorption can be approximated by (Hasegawa & Herbst 1993):

$$k_{\text{crd}}(i, a) = f(T_e(a)) k_{\text{des}}(i, T_e(a)), \quad (11)$$

where $f(T_e(a))$ is an estimation of the fraction of time spent by a grain with radius a at an elevated temperature T_e , defined as the ratio of the cooling timescale by desorption of volatiles to the time interval of successive heating by cosmic-rays. The latter is about 10^6 yrs for $0.1 \mu\text{m}$ grains and cosmic-ray ionization rate of 10^{-17} s^{-1} (Léger et al. 1985); this timescale is inversely proportional to the cross-section of the grain ($\propto a^2$).

The elevated temperature a grain can reach via impulsive heating is also sensitive to the grain size. Cosmic-ray particles deposit more energy when penetrating through larger grains ($\propto a$), but find it difficult to heat up the whole grain to high temperatures due to a larger grain volume. We extend the volumic specific heat formula up to 300 K from Fig. 1 of (Léger et al. 1985),

$$\begin{aligned} C_v(T) &= 1.4 \times 10^3 T^2 \text{ erg cm}^{-3} \text{ K}^{-1}, T < 50 \text{ K}, \\ &= 2.2 \times 10^4 T^{1.3} \text{ erg cm}^{-3} \text{ K}^{-1}, 50 \text{ K} < T < 150 \text{ K}, \\ &= 4.4 \times 10^5 T^{0.7} \text{ erg cm}^{-3} \text{ K}^{-1}, 150 \text{ K} < T < 300 \text{ K}. \end{aligned} \quad (12)$$

The energy deposit to a grain with radius a by impinging Fe nuclei with ~ 20 MeV per nucleon is estimated by

$$\Delta E_{\text{dep}} = 3.8 \times 10^5 \left(\frac{a}{0.1 \mu\text{m}} \right) \text{ eV}, \quad (13)$$

which corresponds to heating up the grains of $0.1 \mu\text{m}$ to 70 K and $0.2 \mu\text{m}$ to 43 K. Smaller grains can reach much higher T_e , e.g., ~ 193 K for $0.03 \mu\text{m}$ grains and over 600 K (extrapolated) for grains $\leq 0.01 \mu\text{m}$.

The subsequent cooling of the grain is mainly achieved through evaporation of CO and other volatile species. According to Hasegawa & Herbst (1993), the evaporation timescale is inversely proportional to k_{des} of CO molecules ($\approx 10^{-5}$ s for $0.1 \mu\text{m}$), which is applicable to grains with enough surface sites for volatile absorbates. From the initial deposited energy ΔE_{dep} , we can estimate the maximum number of CO molecules that would be evaporated into the gas as $N_{\text{evap}} = \Delta E_{\text{dep}} / E_{\text{des}}(\text{CO})$. N_{evap} is usually a small fraction of the total number of surface sites; but for grains smaller than $\sim 0.03 \mu\text{m}$, $N_{\text{evap}} \approx 10^6$ becomes comparable to the number of surface sites (assuming a few ice layers). Therefore, we only apply the scaling of evaporation timescale from Hasegawa & Herbst (1993) to grains with $a \in [0.03, 0.25] \mu\text{m}$, corresponding to a temperature range of about [200, 35] K (hence the final desorption rate has a weak dependence on T_e for a given species, consistent with Hasegawa & Herbst 1993).

For larger grains ($> 0.25 \mu\text{m}$), spot heating by cosmic-rays will start to dominate over whole grain heating (Léger et al. 1985; Shen et al. 2004). For smaller grains with much higher T_e , most CO and other volatile species on the grain surface are rapidly depleted through evaporation with timescale $< 10^{-9}$ s, which only removes $\leq 10\%$ of the total deposited energy E_{dep} . However, because of the high temperature, sublimation of H_2O becomes very efficient (Tielens 2005, each H_2O molecule takes away five times the energy of each CO molecule). The timescale of water sublimation for grains smaller than $0.01 \mu\text{m}$ can be estimated as $\sim 10^{-8}$ s given $T_e \sim 600$ K. For simplicity, these additional processes are not considered in this study (detailed treatment of water sublimation on small grains may potentially affect the abundances of species with large binding energies).

Based on these assumption, the duty cycle can be obtained by scaling both the timescale of evaporative cooling and the time interval between successive heating. The resulting duty cycle $f(T_e(a))$ can vary by more than 10 orders of magnitude (10^{-26} – 10^{-12} s^{-1}) along the standard MRN (Mathis-Rumpl-Nordsieck; Mathis et al. 1977) size distribution; smaller grains have smaller duty cycles per grain because they are struck less frequently by cosmic rays and they spend shorter times at the elevated temperature (see also Acharyya et al. 2011), while larger grains have larger cross-section for incoming cosmic rays and they cool down slowly since their peak temperatures are closer to the ambient gas temperature.

The final value of $\langle k_{\text{crd}}(i) \rangle$ for species i is obtained by averaging over the grain size distribution (weighted by grain surface area) as:

$$\langle k_{\text{crd}} \rangle = \frac{\sum_a k_{\text{crd}} \pi a^2 n(a)}{\sum_a \pi a^2 n(a)}, \quad (14)$$

which is equivalent to treating each surface species as a separate species in each size bin,¹ given enough surface sites for the adsorbed species at each size bin. As an example, the desorption rate $k_{\text{crd}}(\text{CO}, a)$ for CO takes value between $\sim 10^{-17}$ – 10^{-13} s^{-1} for the

¹ The cosmic-ray desorption term in the rate equation Eq. 1 for a size

standard MRN distribution, with larger values of k_{crd} for larger a , and the weighted desorption rate $k_{\text{crd}(i)} \approx 1.04 \times 10^{-14} \text{ s}^{-1}$ (very similar to the values derived by Hasegawa & Herbst (1993) using $0.1 \mu\text{m}$ grains).

Cosmic rays also induce secondary UV photons when interacting with H_2 molecules – the so called H_2 fluorescence in the Lyman and Wemer bands. The resulting flux of UV photons can be estimated by:

$$F_{\text{UV}} \approx 1830 \left(\frac{\zeta^{\text{H}_2}}{10^{-17} \text{ s}^{-1}} \right) \text{ cm}^{-2} \text{ s}^{-1} \quad (15)$$

(Cecchi-Pestellini & Aiello 1992; Ivlev et al. 2015b), assuming the typical interstellar dust gas and dust properties. The corresponding rate of photo-desorption by such a fluorescence can be expressed as,

$$k_{\text{crd,fl}} = \frac{F_{\text{UV}}}{4n_s N_1} Y_i, \quad (16)$$

where $N_1=2$ is the number of ice layers that can be affected by an incoming UV photon for photo-desorption, and Y_i is the photo-desorption yield per photon. For simplicity, we set $Y_i=10^{-3}$ for all desorbing species.

The coupled ODEs (ordinary differential equations) are solved using DVODE library² with sparse matrix turned off, due to the small number of species yet a large number of reactions for each species.

3 RESULT

We evolve the chemical network for 10^5 years for the freeze-out mechanism to take effect (Flower et al. 2005), while the ion chemistry reaches equilibrium as quickly as a few 10^1 years (Caselli et al. 2002b). In the high density regions, we adopt a barotropic equation of state (EOS) described in Appendix A to mimic the change of temperature at high densities including those for protostellar disks. The cosmic-ray ionization rate ($\zeta_0^{\text{H}_2} = 1.3 \times 10^{-17} \text{ s}^{-1}$) also attenuates exponentially at high densities following the relation given in Nakano et al. 2002 (see also, Eq. 1 in Zhao et al. 2016), until a lower limit of $1.1 \times 10^{-22} \text{ s}^{-1}$ (corresponding to the ionization by radioactive decay of long-lived ^{40}K) is reached.

In this section, we demonstrate that grain size distribution can significantly affect cosmic-ray desorption as well as non-ideal MHD effects. In particular, (1) the abundance differentiation among volatile species is sensitive to the maximum grain size ($a_{\text{max}} > 0.1 \mu\text{m}$); (2) ambipolar diffusivity is sensitive to the amount of VSGs (a few to tens of nanometer, see also Zhao et al. 2016); (3) Hall diffusivity is generally sensitive to grain size distribution in terms of sign and magnitude, but reaches a maximum level at densities below 10^{13} cm^{-3} when $a_{\text{min}} \approx 0.04 \mu\text{m}$ (in contrast to Dzyurkevich et al. 2017).

3.1 Amplified Differential Depletion of Volatile Species Due to Cosmic-ray Desorption

Conventionally, the small difference in binding energies among volatile species are considered to have negligible effect on their gas-

distribution is,

$$\Sigma_a \left[k_{\text{crd}(a)} \frac{n_{i,s}}{\Sigma_a \pi a^2 n(a)} \pi a^2 n(a) \right] = \langle k_{\text{crd}} \rangle n_{i,s}$$

² available at <http://www.radford.edu/~thompson/vodef90web/>

phase abundances. However, with the new formulation of cosmic-ray desorption rate which includes the dependence on grain size, the effect of binding energies on the abundances of volatiles is amplified by the variations in the elevated temperature. As a result, the small difference in binding energies can be the origin of the differential depletion among volatiles in this paradigm.³

Fig. 1 shows the abundances of the main ion and neutral species relative to H_2 using the new formulation of cosmic-ray desorption rate (Eq. 11). With the standard MRN size distribution, the gas-phase atomic N is two orders of magnitude more abundance than gas-phase CO (in the density range between a few 10^5 and a few 10^{10} cm^{-3}), while the abundances of N_2 and O_2 are higher than CO by a factor of few (consistent with observational constraints by Maret et al. 2006; see also van Dishoeck & Blake 1998). The excess of N_2 over CO in the gas phase also leads to an excess of N_2H^+ over HCO^+ by a factor of a few in the density range of dense cores. In contrast, when the conventional pre-factor for the cosmic-ray desorption rate $f(70 \text{ K}) = 3.16 \times 10^{-19}$ (derived with $0.1 \mu\text{m}$ grains) is used instead, the difference in abundances among volatile species becomes almost negligible (Fig. 2), which recovers the claims of existing studies (e.g., Flower et al. 2005).

The differential depletion of volatile species is clearly amplified by adopting the new cosmic-ray desorption rate that varies with grain sizes. Fig. 3 compares for the main volatile species the cosmic-ray desorption rates $k_{\text{crd}(i, a)}$ (computed via Eq. 11–13) and the averaged value $\langle k_{\text{crd}(i)} \rangle$, along with the conventional rate for $0.1 \mu\text{m}$ grain from Hasegawa & Herbst (1993). Apparently, the averaged desorption rates $\langle k_{\text{crd}(i)} \rangle$ (circled crosses in Fig. 3) of different volatile species are more separated from each other than the conventional desorption rates computed using $0.1 \mu\text{m}$ grain (dashed horizontal lines). The enhanced differential depletion is caused by the large variation of $k_{\text{crd}(i, a)}$ (among different species) in the grain size range larger than $\sim 0.1 \mu\text{m}$; these grains are only heated by cosmic rays to lower elevated temperatures $T_e(a)$ (e.g. $\sim 40 \text{ K}$) and are more sensitive to the difference in binding energies among volatile species. For example, $k_{\text{crd}(i, 0.2 \mu\text{m})}$ of volatile species with small binding energies (e.g., N and N_2) reaches $\sim 10^{-11} - 10^{-10} \text{ s}^{-1}$, compared to 10^{-15} s^{-1} for less volatile species (e.g., O). Therefore, the averaged $\langle k_{\text{crd}(i)} \rangle$ (weighted by grain surface area) lean towards larger values for more volatile species (e.g., N and N_2) but smaller values for less volatile species (e.g., O, H_2O). We have also tested models with longer evolution time 10^6 yrs and 10^7 yrs, and the effect of differential depletion is almost identical.

Note that on the freeze-out timescale ($\sim 10^5$ yrs), the majority of desorption of volatile species ($E_{\text{des}} \sim 1000 \text{ K}$ such as CO, N_2 , O_2 , C, N, and O) owes to the impulsive heating by cosmic-rays. In comparison, the cosmic-ray induced UV photons contribute most to the desorption of species such as OH and H_2O that have large binding energies E_{des} . Indeed, $k_{\text{crd}(i, a)}$ is a decreasing function of a at larger grain sizes, because the evaporative cooling timescale is derived by assuming CO as the primary volatile species to cool the grains (Hasegawa & Herbst 1993), and within the duty cycle, the non-volatile species are difficult to evaporate into gas-phase when the elevated temperature is low. A more strict treatment for the evaporative cooling process including the contributions from both CO and H_2O ice may provide more accurate results for these non-volatile species. Again, we are aware of the disagreements over

³ Indeed, more complete chemical networks including grain surface reactions are needed to fully understand the differential depletion of volatile species in dense molecular clouds; we will leave it to future investigations.

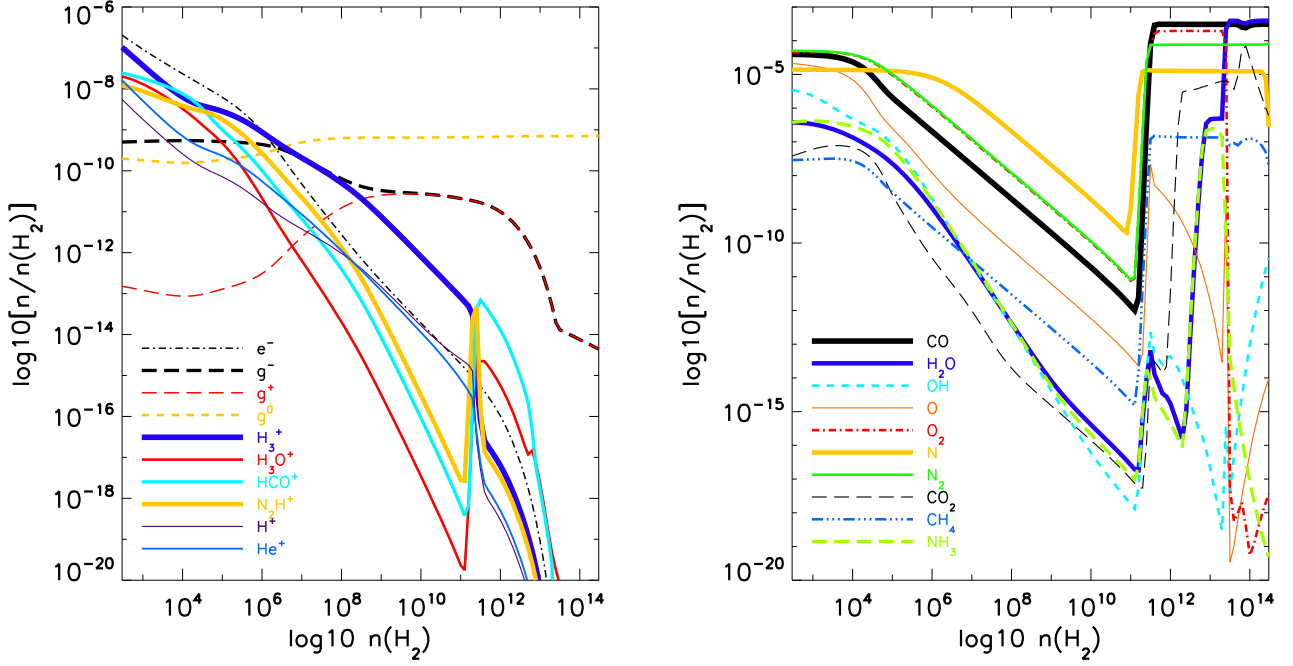


Figure 1. Fractional abundances of the main ion and neutral species computed with the new formulation of cosmic-ray desorption rate for a standard MRN size distribution. In the right panel, N atom is ~ 2 orders of magnitude more abundant than CO for number densities between 10^5 – 10^{11} cm^{-3} .

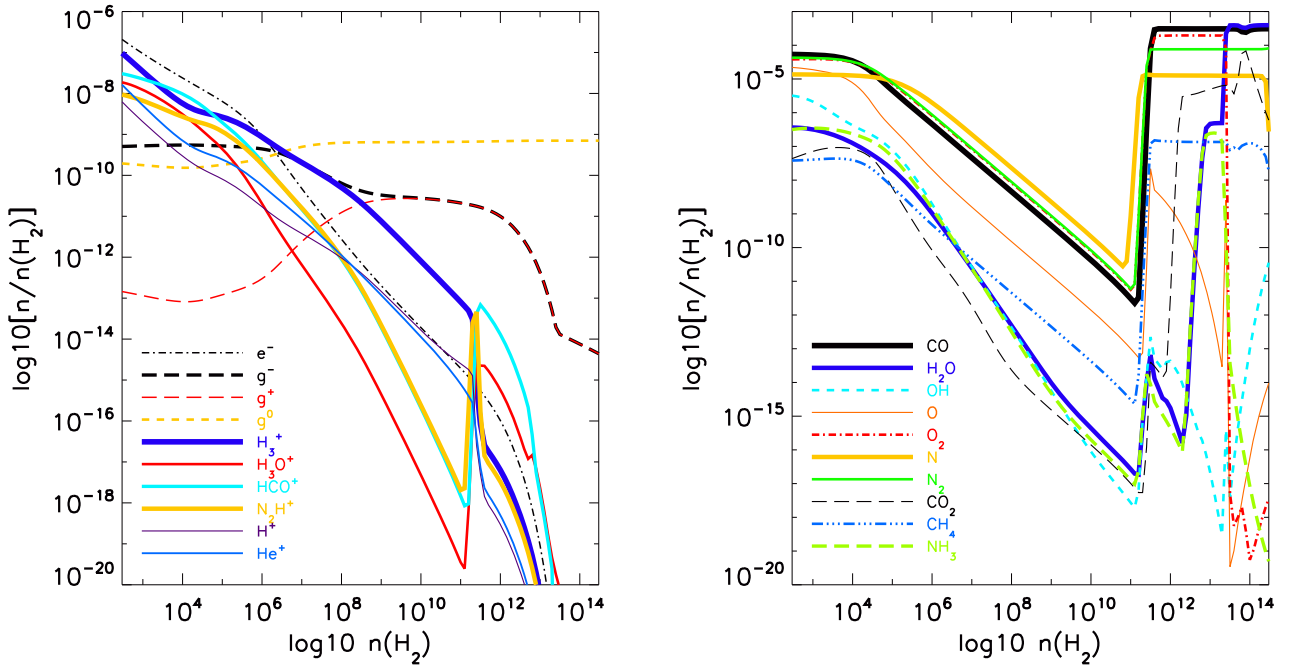


Figure 2. Fractional abundances of the main ion and neutral species computed with the conventional $f(70\text{ K})$ pre-factor. Other parameters remain the same as in Fig. 1. The abundances of volatile species in the right panel are nearly indistinguishable from each other.

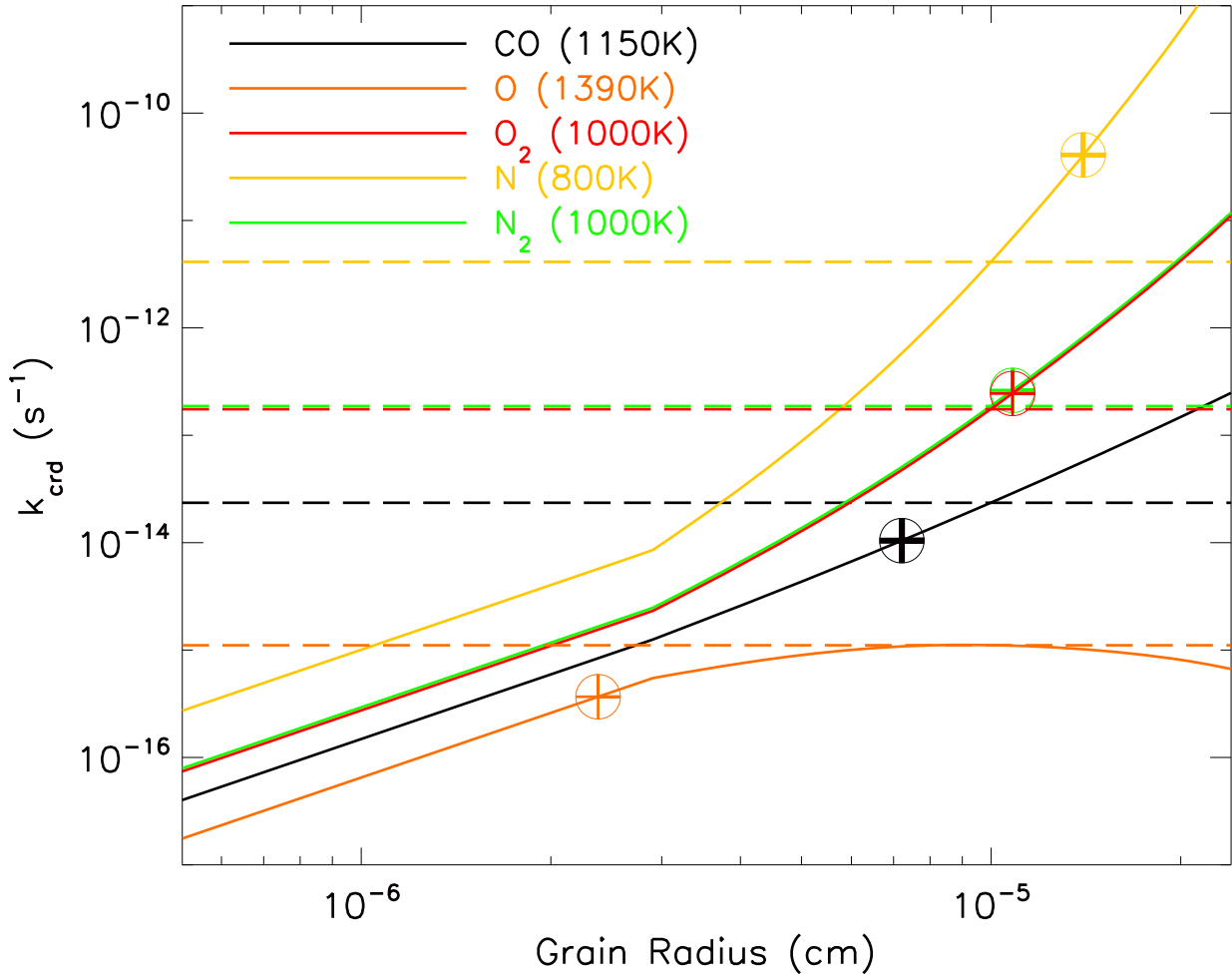


Figure 3. Comparison of cosmic-ray desorption rates among volatile species. Solid lines represent the desorption rate per grain $k_{\text{crd}}(i, a)$ for a given species i and grain radius a . The circled crosses mark the averaged desorption rate for each species. Long dashed lines are the desorption rate computed using the conventional $f(70 \text{ K})$ pre-factor. The value of binding energies are taken from Sipila et al. (2015).

binding energies among existing literature, and improved measurements of binding energies (e.g. Cazaux et al. 2017; Shimonishi et al. 2018) are needed to refine the cosmic-ray desorption model presented here.

3.2 Freeze-Out and Relative Abundance of Ions

As shown in § 3.1 above, the chemical abundances are strongly affected by the freeze-out and desorption processes. In particular, the dominant ion species in dense cores is no longer the commonly assumed HCO^+ (Fig. 4a; see also Umebayashi & Nakano 1990; Zhao et al. 2016; Marchand et al. 2016) but H_3^+ instead for number densities below 10^{11} cm^{-3} for the standard MRN size distribution (see Fig. 1 above), consistent with the result of Flower et al. (2005).

However, the grain size distribution can also affect the relative abundances among ion species via the change of surface area for freeze-out. As shown in Fig. 4b, when using a truncated MRN distribution with $a_{\text{min}}=0.1 \mu\text{m}$, H_3^+ only starts to dominate the ion

abundances for densities between 10^8 – 10^{11} cm^{-3} . In the low density regime, HCO^+ is still the most abundant ion species up to $\sim 8 \times 10^6 \text{ cm}^{-3}$, when N_2H^+ overtakes HCO^+ . In comparison, with the standard MRN distribution (Fig. 1), N_2H^+ starts to dominate over HCO^+ at relatively low densities $\sim 5 \times 10^4 \text{ cm}^{-3}$, but they both are much less abundant than H_3^+ (10^5 – $10^{11} \text{ cm}^{-3} \text{ cm}^{-3}$). It is likely that neither size distributions can well characterize the grain properties in dense cores over the long time evolution (e.g., Hirashita 2012). We also show an intermediate case with $a_{\text{min}}=0.04 \mu\text{m}$ in Appendix C, the dominant ion species switches from HCO^+ to N_2H^+ at number density around $8 \times 10^5 \text{ cm}^{-3}$, and H_3^+ dominates over both between 5×10^6 – 10^{11} cm^{-3} . The change of the dominant ion species is regulated by the level of depletion of volatile species (e.g., CO and N_2), which is sensitive to the grain surface area for freeze-out.

Observationally, the relative abundances among the main ion species may provide an alternative way of determining the average grain size $\langle a \rangle$ in dense cores. For instance, if the abundance of H_3^+ could be inferred either directly or via comparison of H_2D^+ and

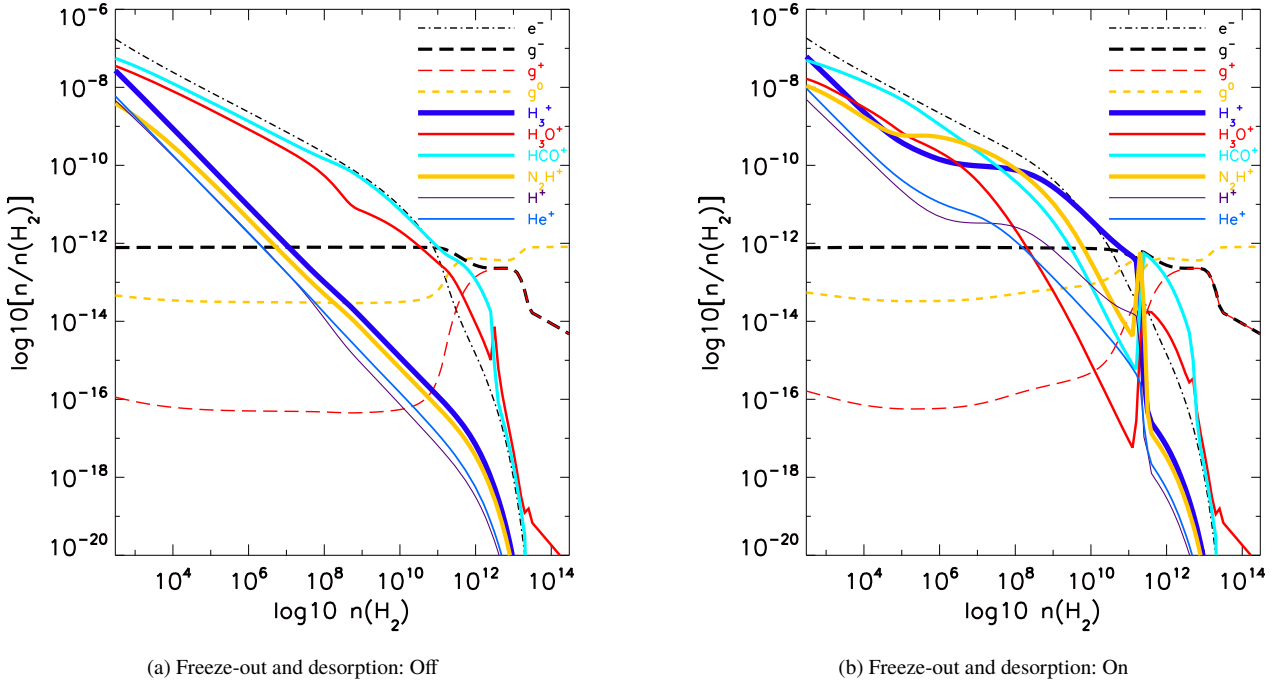


Figure 4. Fractional abundances of the main ion species computed without freeze-out/desorption (left panel) and with freeze-out/desorption (right panel) for the truncated MRN size distribution with $a_{\min}=0.1 \mu\text{m}$.

other molecular ion observations with chemical models, one can obtain an estimate of the grain size by comparing the abundance of H_3^+ with that of N_2H^+ (or HCO^+) at given densities (slightly larger $\langle a \rangle$ makes it harder for H_3^+ to dominate over the other two ions). Furthermore, with a proper limit on the maximum grain size constrained by existing observations (if any), the minimum grain size can be inferred (assuming a certain power law index for the size distribution), and vice versa.

3.3 Effect of Chemistry on Non-ideal MHD Diffusivities

With the ionization fraction from the chemical network, it is straightforward to obtain the three non-ideal MHD diffusivities: η_{AD} , η_{Ohm} , η_{Hall} (Appendix B; see also, Wardle & Ng 1999; Zhao et al. 2016). Despite the pronounced effect of freeze-out and desorption processes on the abundance of ions, they only have limited influence on the non-ideal MHD effects that are instead modulated by the grain size distribution (Wardle & Ng 1999; Padovani et al. 2014; Zhao et al. 2016; Dzyurkevich et al. 2017). However, disagreement still exists among literatures in terms of the effect of grain size on magnetic diffusivities. We now utilize our chemical network to clarify the disagreement, with a particular emphasis on Hall diffusivity, which is not covered in details in Zhao et al. (2016).

3.3.a Limited Influence of Freeze-out and Desorption on Magnetic Diffusivities

We again vary the minimum grain size a_{\min} of the size distribution, but keep the power index of -3.5 and $a_{\max} = 0.25 \mu\text{m}$. Similar to Li et al. (2011) and Zhao et al. (2016), we adopt the simple relation

between magnetic field and density (Nakano et al. 2002),

$$|B| = 0.143 \left[\frac{n(\text{H}_2)}{\text{cm}^{-3}} \right]^{0.5} \mu\text{G}, \quad (17)$$

to estimate the magnetic field strength. The resulting magnetic diffusivities for different grain sizes are shown in Fig. 5, with freeze-out/desorption turned on or off. Overall, the magnetic diffusivities are very similar between the two cases, indicating that changes in ion abundances⁴ due to freeze-out and/or desorption only have limited effect on the magnetic diffusivities.

The most obvious difference between the two cases is the Hall diffusivity in the density range $\sim 10^9\text{--}10^{11} \text{cm}^{-3}$ when using $a_{\min} = 0.1 \mu\text{m}$. In the case without freeze-out and desorption, η_{Hall} briefly switches to positive sign in the vicinity of 10^{10}cm^{-3} , causing a wider density range ($\sim 10^9\text{--}10^{11} \text{cm}^{-3}$) to have lowered values of η_{Hall} . In contrast, the case with freeze-out and desorption (bottom panels of Fig. 5) shows a more smooth negative value of η_{Hall} in the similar density range. The reason for such a difference is evident when comparing Fig. 6 and Fig. 7 where we plot the contributions of the main charged species to the three components of fluid conductivity (parallel σ_{\parallel} , Pedersen σ_{p} , and Hall σ_{H} defined in Appendix B). The principal term that determines Hall diffusivity is the Hall conductivity σ_{H} , which carries a sign for each charged species (Eq. B6). In the case without freeze-out and desorption, σ_{H} becomes positive near 10^{10}cm^{-3} because the total contribution of σ_{H} from ions (especially HCO^+ and H_3O^+) surpasses $\sigma_{\text{H}}(g^-)$. However, when freeze-out and desorption are turned on, σ_{H} is always dominated by g^- in low density regimes ($\lesssim 10^{11} \text{cm}^{-3}$). In fact, when we adopt $a_{\min} \approx 0.15 \mu\text{m}$ for the freeze-out/desorption

⁴ The change in Hall parameter (defined in Appendix B) by switching the dominant ion species from HCO^+ to H_3^+ has even less effect ($\lesssim 5\%$).

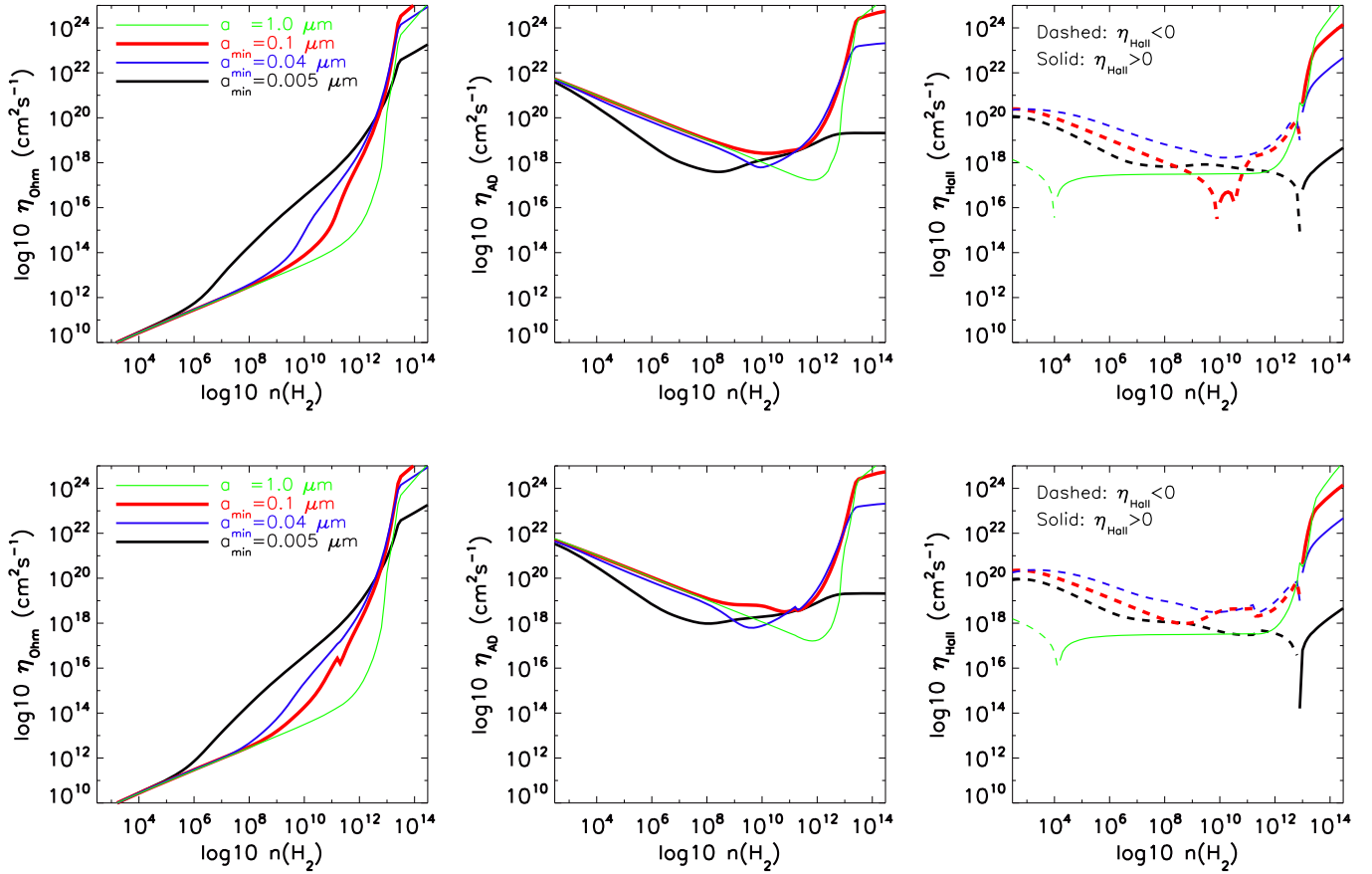


Figure 5. Non-ideal MHD diffusivities computed without (top three panels) and with (bottom three panels) freeze-out/desorption for different size distributions with $a_{\min} = 0.005 \mu\text{m}$ (MRN: black), $a_{\min} = 0.04 \mu\text{m}$ (blue), $a_{\min} = 0.1 \mu\text{m}$ (red), $a = 1.0 \mu\text{m}$ (green). Ambipolar diffusion is at a maximum level over the density range when $a_{\min} = 0.1 \mu\text{m}$, while Hall effect is more efficient for disk formation when $a_{\min} = 0.04 \mu\text{m}$.

case, η_{Hall} presents similar sign change between 10^9 – 10^{10} cm^{-3} . Therefore, it is a general behavior of Hall diffusivity that rather depends on the choice of grain size than on freeze-out/desorption. As grain size increases, the abundance of g^- reduces, so that positive Hall diffusivity extends to wider and wider regions in the lower density regime ($\lesssim 10^{11} \text{ cm}^{-3}$).

3.3.b Optimal Grain Size for Hall Diffusivity

In fact, there exists an optimal grain size $a_{\min} \approx 0.04 \mu\text{m}$ for which Hall diffusivity η_{Hall} reaches a maximum level at number densities below $\lesssim 10^{11} \text{ cm}^{-3}$. According to Eq. B3 in Appendix B, large η_{Hall} requires both Hall conductivity σ_{H} and Pedersen conductivity σ_{P} to be small, and at the same time $\sigma_{\text{H}} \geq \sigma_{\text{P}}$. As shown in Fig. 8 for $a_{\min} \approx 0.04 \mu\text{m}$, the two conductivity components σ_{H} and σ_{P} are roughly equal to each other ($\lesssim 10^{11} \text{ cm}^{-3}$). The Hall diffusivity η_{Hall} reaches a maximum here because (1) for larger $a_{\min} (\geq 0.04 \mu\text{m})$, σ_{H} starts to decrease below σ_{P} , and (2) for smaller $a_{\min} (\leq 0.04 \mu\text{m})$, σ_{H} increases first and followed by the increase of σ_{P} ($\leq 0.01 \mu\text{m}$). η_{Hall} tends to be reduced either way. The key is that Hall conductivity σ_{H} generally increases with decreasing abundance of g^- , and Pedersen conductivity σ_{P} starts to be significantly dominated by VSGs when $a_{\min} \lesssim 0.02 \mu\text{m}$. Note that the trend presented here is essentially

the same as that shown in Appendix A of Zhao et al. (2016), except that the main focus was previously ambipolar diffusivity.

At high densities ($\geq 10^{13} \text{ cm}^{-3}$), the Hall diffusivity is mostly positive and increases monotonically with increasing grain size. More specifically, the overall magnitude of Hall diffusivity at densities $\geq 10^{11} \text{ cm}^{-3}$ (protostellar disk density) is quite low when $a_{\min} \lesssim 0.01 \mu\text{m}$; and it increases by a few orders of magnitude when $a_{\min} \geq 0.02 \mu\text{m}$. It is consistent with the behaviors of Pedersen and Hall conductivities in this grain size range.

3.3.c Comparison with Other Work

Comparing our result of Hall diffusivity with that of Dzyurkevich et al. (2017), we agree on the fact that larger grain sizes ($> 0.1 \mu\text{m}$) greatly reduces the Hall diffusivity due to the reduction of the abundance of g^- and hence $\sigma_{\text{H}}(g^-)$. However, we do notice a few differences:

- (1) The existence of a maximum level of Hall diffusivity (for number densities $\lesssim 10^{11} \text{ cm}^{-3}$) when $a_{\min} \approx 0.04 \mu\text{m}$ (or $< a \approx 0.063 \mu\text{m}$) is not discussed in Dzyurkevich et al. (2017).
- (2) The sign of Hall diffusivity becoming negative (for number densities $\lesssim 10^{11} \text{ cm}^{-3}$) applies to all cases with $a_{\min} \lesssim 0.1 \mu\text{m}$ (or $< a \approx 0.14 \mu\text{m}$). In contrast, Dzyurkevich et al. (2017) show that

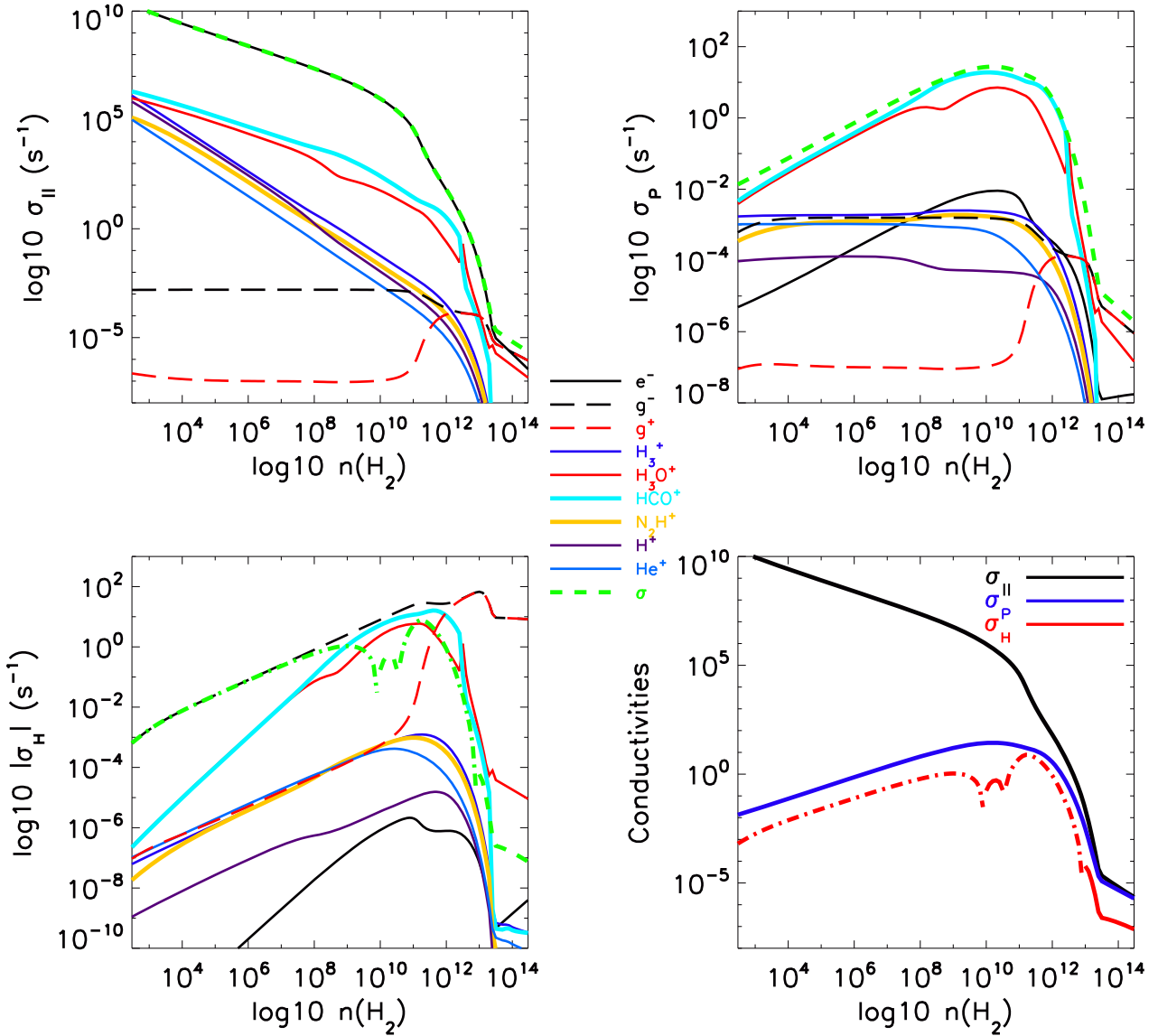


Figure 6. Components of conductivity tensor and the contributions from major charged species, for the truncated MRN size distribution with $a_{\min} = 0.1 \mu\text{m}$ and $a_{\max} = 0.25 \mu\text{m}$, with freeze-out and desorption turned off.

the behavior of Hall diffusivity η_{Hall} (as well as η_{Ohmic} and η_{AD}) in the cases with $\langle a \rangle = 0.05 \mu\text{m}$ and $\langle a \rangle = 0.1 \mu\text{m}$ are almost identical to each other (their Fig. 2), which is different from what we found using our network: η_{Hall} in their two cases differs by more than 1 order of magnitude; the sign change only occurs in the case with $\langle a \rangle = 0.1 \mu\text{m}$ but not for $\langle a \rangle = 0.05 \mu\text{m}$.

(3) The statement in Dzyurkevich et al. (2017) that Hall effect always dominates ambipolar diffusion for grain sizes below⁵ $0.02 \mu\text{m}$ is no longer true when $a_{\min} < 0.004 \mu\text{m}$. Recall that (§ 3.3.b; see also Zhao et al. 2016) σ_{H} starts to increase when a_{\min} drops below $0.04 \mu\text{m}$, yet σ_{\perp} increases more rapidly when $a_{\min} < 0.02 \mu\text{m}$

⁵ We obtain a value of $a_{\min} \sim 0.03 \mu\text{m}$ (or $\langle a \rangle = 0.048 \mu\text{m}$) for the similar effect, but the Hall effect only dominates over AD in a limited density range near 10^8 cm^{-3} .

and becomes larger than σ_{H} when $a_{\min} < 0.004 \mu\text{m}$. Therefore, AD regains the dominance over Hall effect as tiny grains with size comparable to PAHs are included, but neither diffusivities are large enough for efficient magnetic decoupling. For example, Fig. 9 shows the magnetic diffusivities for a size distribution with $a_{\min} = 10$, where both η_{AD} and η_{Hall} are orders of magnitude smaller than the models with larger a_{\min} (Fig. 5).

Besides the Hall diffusivity, the result of Ohmic and ambipolar diffusivity (first two panels of Fig. 5) is essentially the same as in Zhao et al. (2016) computed using a more simplified network (see their § 4.2, § 4.4, and Appendix A). The main result remains the same: removal of VSGs (a few to tens of nanometer) significantly enhances the ambipolar diffusivity. Note that we incorporated a barotropic EOS in this work, hence the high temperature in the high density regime ($\gtrsim 10^{11} \text{ cm}^{-3}$) causes the magnetic diffusivities to

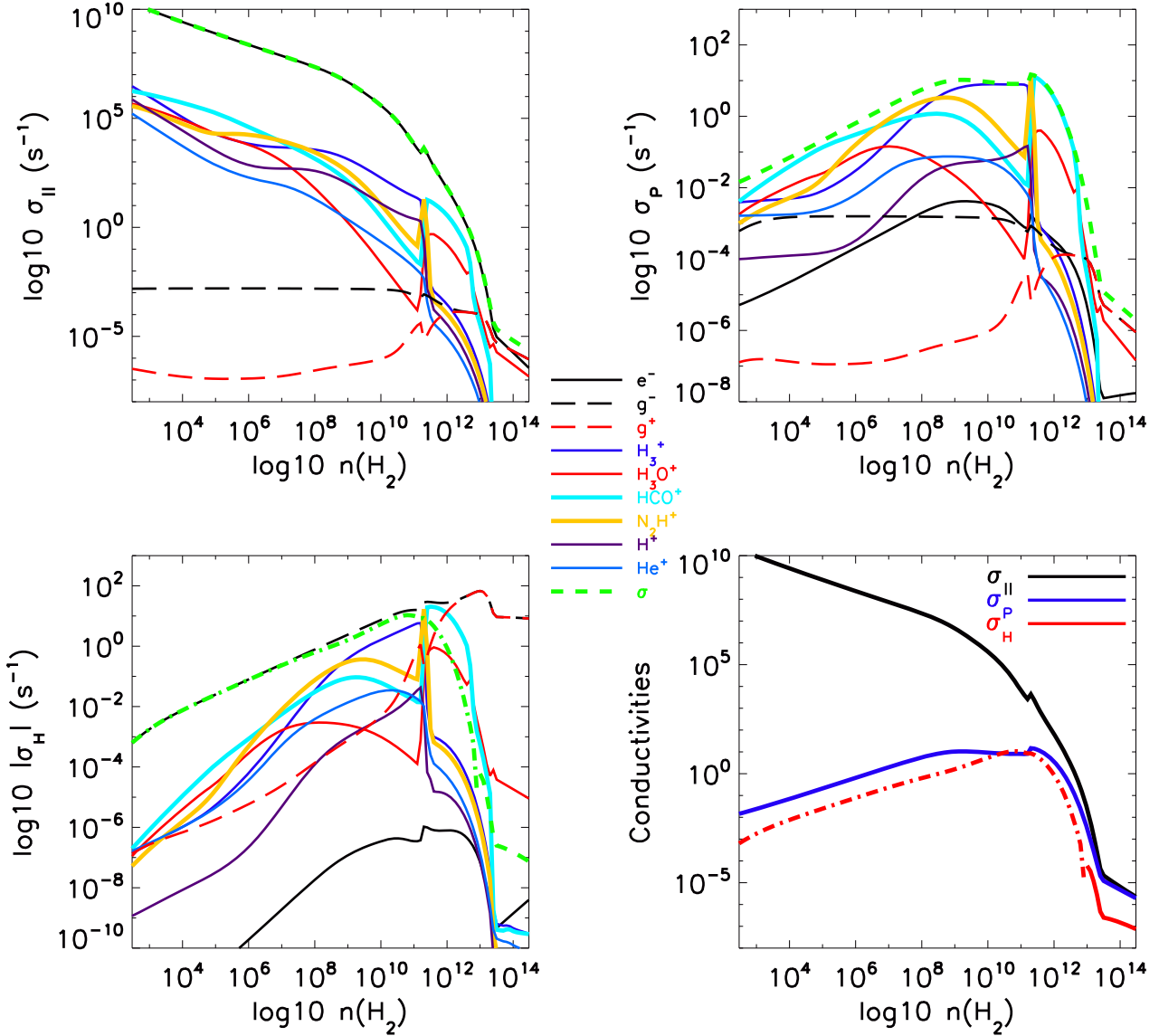


Figure 7. Same as Fig. 6, but with freeze-out and desorption turned on.

be higher than the values shown in Zhao et al. (2016) that assumes a constant T of 10 K. In fact, when the same EOS is used, the results from the two networks almost overlap with each other, which validates the convergence of both chemical networks.

To summarize, the magnetic diffusivities are very sensitive to the grain size distribution. In the low density regime ($<10^{10} \text{ cm}^{-3}$) where the diffusion of magnetic fields matters the most for disk formation and growth, ambipolar diffusivity η_{AD} reaches a maximum level for disk formation when the MRN size distribution is truncated at $0.1 \mu\text{m}$, and Hall diffusivity η_{Hall} reaches a maximum level when the distribution is truncated at $0.04 \mu\text{m}$.⁶ Note that when choosing

$a_{\text{min}} = 0.04 \mu\text{m}$, the resulting η_{AD} is not far from its maximum level with $a_{\text{min}} = 0.1 \mu\text{m}$. Nevertheless, the presence of VSGs reduces the strength of both ambipolar and Hall diffusivities. Furthermore, the Ohmic dissipation only becomes comparable to the other two effects at very high densities (a few $\sim 10^{12} \text{ cm}^{-3}$), similar to the conclusions of other work (e.g., Zhao et al. 2016; Marchand et al. 2016).

⁶ The optimal grain size for Hall effect also depends slightly on the cosmic-ray ionization rate $\zeta_0^{\text{H}_2}$, which changes to $a_{\text{min}} \sim 0.03 \mu\text{m}$ for $\zeta_0^{\text{H}_2} = 5.0 \times 10^{-17} \text{ s}^{-1}$ and $a_{\text{min}} \sim 0.07 \mu\text{m}$ for $\zeta_0^{\text{H}_2} = 1.0 \times 10^{-18} \text{ s}^{-1}$ (not shown).

However, the magnitude of η_{AD} roughly scales with $1/\sqrt{\zeta}$ and the optimal grain size of $0.1 \mu\text{m}$ stays the same for different $\zeta_0^{\text{H}_2}$.

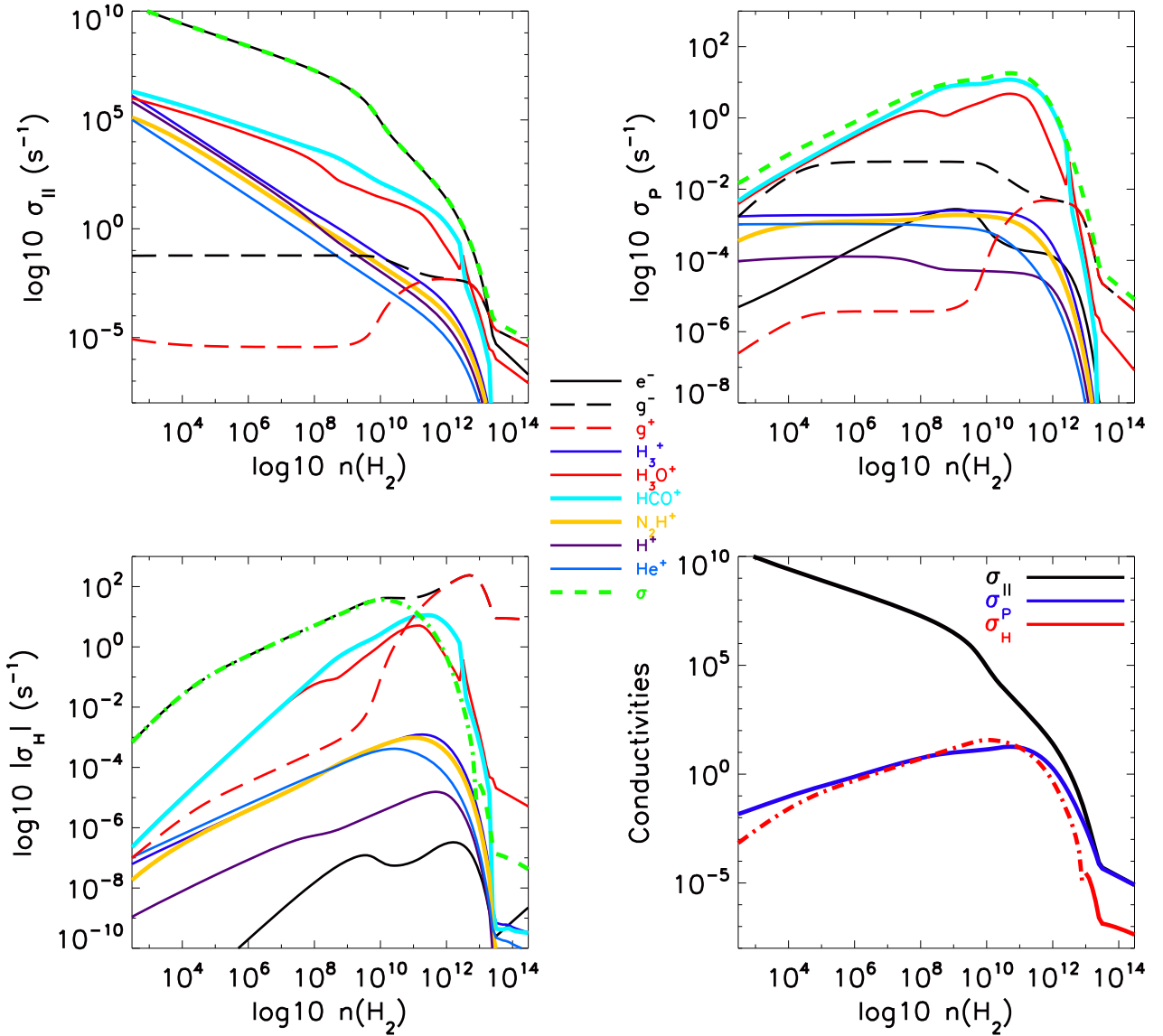


Figure 8. Components of conductivity and the contributions from major charged species, for the truncated MRN size distribution with $a_{\min} = 0.04 \mu\text{m}$ and $a_{\max} = 0.25 \mu\text{m}$. This size distribution produces the strongest Hall effect (at densities $\lesssim 10^{11} \text{cm}^{-3}$). Freeze-out and desorption are turned off.

3.4 Chemical Abundances at High Densities: Tracers for Protostellar Disks

By including the barotropic EOS (Appendix A), thermal desorption of molecules due to an increased gas temperature is simultaneously modeled with the chemical network, which can be used to analyze the chemical tracers in protostellar disks. As shown in Fig. 1, thermal desorption efficiently operates for most species at densities \gtrsim a few 10^{11}cm^{-3} , above which neutral-neutral reactions dominate the chemistry. At number densities between 10^{12} – 10^{13}cm^{-3} , the main gas-phase species are CO, O₂, N, N₂, CO₂, and a small fraction of CH₄. As temperature rises even higher (~ 200 – 300K) at number densities $>10^{13} \text{cm}^{-3}$, H₂O start to return to gas-phase via thermal desorption, and most O₂ are turned into CO₂ by reacting with CO. But the abundances of CO₂, N and CH₄ continue to decrease towards even higher densities beyond the range considered here,

leaving only CO, H₂O and N₂ as the most abundant species in early protostellar disks (see also, e.g., Molyarova et al. 2017) based on our network. Note that grain surface chemistry is very important for the more complex species (e.g. CH₃OH and other complex organic molecules) which best trace the high density and warm regions surrounding the central protostar, including protostellar disks; we will describe this more detailed chemical work in a future paper.

In comparison, the fractional abundances of ions at high densities are more than ten orders of magnitude lower than the major neutral species. Our result shows that HCO⁺ remains as a good ionic tracer in the bulk part of the protostellar disk, along with H₃O⁺ which is hard to observe. N₂H⁺ should only trace the outer part of the disk and show as a ring structure. Note that the ionization fraction presented here is regulated by the simple exponential attenuation of cosmic-rays; improving the cosmic-ray attenuation

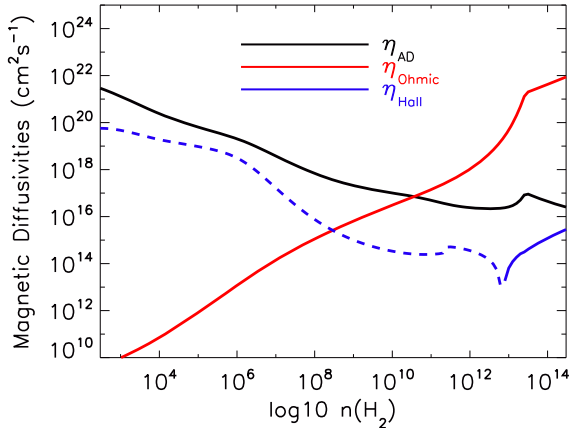


Figure 9. Magnetic diffusivities computed with freeze-out/desorption for $a_{\min} = 10$ (mimic a population of PAHs).

function or including other sources of ionization (e.g., X-ray, thermal ionization; see [Armitage 2011](#); [Bai 2011a](#)) should provide a more realistic ionization fraction in different parts of the protostellar disk. We will explore such topics in an upcoming work.

4 DISCUSSION & SUMMARY

The new chemical network presented here is still under development, with a few main ingredients to be implemented, including multiple grain charging (e.g., [Ivlev et al. 2016](#)), grain surface chemistry (e.g., [Harada et al. 2017](#)). Multiple charging becomes important for large grains at high temperature (e.g., [Draine & Sutin 1987](#)), and should be investigated in detail for our modeling of protoplanetary disks next.

We noticed that a parallel work by [Iqbal & Wakelam \(2018\)](#) that includes grain surface chemistry also uses a similar formulation of cosmic-ray desorption rate. However, they assume a constant evaporative cooling timescale of 10^{-5} s for all grain sizes, which leads to a significant over-estimation of the impact of small grains on the gas-phase abundances (cosmic-ray desorption rate increased by many orders of magnitude for all species). In fact, the chemical abundances computed using the conventional pre-factor $f(70\text{ K})$ is already quite high compared to observations (see Fig. 9 of [Shen et al. 2004](#)). As stated by [Hasegawa & Herbst \(1993\)](#), the evaporative cooling timescale is inversely proportional to k_{des} , and the value of 10^{-5} s is only suitable for $0.1\ \mu\text{m}$ with 70 K. For grains with enough surface sites ($>0.03\ \mu\text{m}$), this timescale can be properly calculated using different T_e for the given grain size a (see § 2.1). Within the size range $[0.03, 0.25]\ \mu\text{m}$, slightly small grains can be cooled down by tens of K from the peak temperature (T_e) by evaporating only $\sim 10^5$ CO molecules, while the temperature of larger grains is difficult to reduce, with the reduction of a few K requiring the evaporation of a few 10^6 CO molecules (values obtained by integrating Eq. 12). Therefore, larger grains stay at their elevated temperatures for a much longer time, allowing a sufficient desorption of volatile species from their surfaces. In comparison, the peak temperature of small grains is so high that the majority of CO and other volatiles evaporate almost instantly, the small grain then cools down via sublimation of H_2O while desorbing other non-volatile

species. Nonetheless, the evaporation timescale of volatile species on small grains should be rather rapid.

Furthermore, according to the formulation by ([Hasegawa & Herbst 1993](#)), the rate of cosmic-ray desorption should have a weak dependence on T_e for a given species, since both the duty cycle $f(T_e(a))$ and the desorption rate $k_{\text{des}}(i, T_e(a))$ in Eq. 11 have similar exponential dependence on T_e . Adopting a constant evaporating cooling time of 10^{-5} s for 70 K alone but much higher $T_e(a)$ K in $k_{\text{des}}(i, T_e(a))$ is responsible for the large effect of cosmic-ray desorption on the chemical abundances shown in [Iqbal & Wakelam \(2018\)](#). Nevertheless, our new formulation of cosmic-ray desorption is still based on [Hasegawa & Herbst \(1993\)](#) and [Acharyya et al. \(2011\)](#), which is a crude approximation to the stochastic process of impinging cosmic-ray particles on grain surfaces.

Despite the simplified chemical model we adopted here, we are able to extract a few novel effects of the grain size distribution on the desorption of volatile species and on the non-ideal MHD diffusivity, along with the key factors operating behind these effects:

(1) The rate of direct desorption of volatile species by cosmic-ray from grains with different sizes can vary by many orders of magnitude over the range of grain size in the standard MRN size distribution, due to the large difference in the elevated temperature of grains of different sizes, instead of a constant 70 K ([Hasegawa & Herbst 1993](#)).

(2) The desorption of volatile species by cosmic-ray is very sensitive to the presence of grains larger than $0.1\ \mu\text{m}$, because they are heated by cosmic-ray to a lower temperature (~ 40 K) and the difference in desorption rates among volatile species due to the slight difference in binding energies is amplified. The resulting chemical abundances show an increased amount of nitrogen bearing species in the gas-phase. Particularly, atomic nitrogen N is about two orders of magnitude more abundant than CO, while gas-phase N_2 is a few times more than CO. Accordingly, N_2H^+ becomes a more abundant tracer than HCO^+ in dense cores, which provides a natural way to explain the well known difference between the distribution of CO and N_2 related molecules (such as N_2H^+) in dense cores (e.g., [Caselli et al. 2002a,b](#)).

(3) Small grains ($\lesssim \text{few } 100$) dominate the cosmic-ray desorption rate of non-volatile species such OH and H_2O . However, for such species, direct cosmic-ray desorption is much less efficient than the desorption by cosmic-ray induced UV photons.

(4) Freeze-out of molecules changes the dominant ion in dense cores from the commonly assumed HCO^+ to H_3^+ , yet the relative abundance between H_3^+ and HCO^+ (N_2H^+) at given densities also changes with grain size. The relation of ion densities, if observed, may provide a potential way to constrain the grain size in dense cores. Besides, the change in the dominant ion species in the gas-phase has very limited effect on the magnetic diffusivities.

(5) The magnetic diffusivities are highly dependent on the grain size distribution. We confirm the role of VSGs in weakening the efficiency of both ambipolar diffusion ([Padovani et al. 2014](#); [Zhao et al. 2016](#)) and Hall effect with or without freeze-out and desorption. At densities below $\sim 10^{10}\ \text{cm}^{-3}$, the maximum ambipolar diffusion is achieved when using a truncated MRN size distribution with $a_{\min} \sim 0.1\ \mu\text{m}$; and to reach a maximum Hall effect, $a_{\min} \sim 0.04\ \mu\text{m}$ is optimal.

Our chemical network can be either tabulated to provide the magnetic diffusivities for non-ideal MHD simulations or used to post-process the simulation results of dense cores and protostellar disks. Although much work remains to be done, our results have shown that grain evolution in dense molecular clouds has a profound

influence on both the chemical and dynamical evolution of the system, which deserves more self-consistent study in the future.

ACKNOWLEDGEMENTS

We thank Wing-Fai Thi, Seyit Höcük, and Olli Sipilä for inspiring discussions. BZ and PC acknowledge support from the European Research Council (ERC; project PALs 320620). Z.-Y. L. is supported in part by NASA NNX14AB38G and NSF AST-1716259.

APPENDIX A: EQUATION OF STATE

We use a broken power law profile for the equation of state (EOS), fitted to mimic the radiative transfer results of Tomida et al. (2013):

$$T = \begin{cases} T_0 + 1.5 \frac{\rho}{10^{-13}} & \text{for } \rho < 10^{-12} \\ (T_0 + 15) \left(\frac{\rho}{10^{-12}} \right)^{0.6} & \text{for } 10^{-12} \leq \rho \leq 10^{-11} \\ 10^{0.6} (T_0 + 15) \left(\frac{\rho}{10^{-11}} \right)^{0.44} & \text{for } 10^{-11} \leq \rho \leq 3 \times 10^{-9} \end{cases} \quad (\text{A1})$$

where $T_0 = 10$ K. The comparison for different EOS is shown in Fig. A1. The same EOS is adopted in the study of disk formation by Zhao et al. (2018).

APPENDIX B: MAGNETIC DIFFUSIVITY AND CONDUCTIVITY

The three non-ideal MHD coefficients can be expressed in terms of the components of the conductivity tensor σ (e.g., Wardle 2007):

$$\eta_{\text{AD}} = \frac{c^2}{4\pi} \left(\frac{\sigma_{\text{P}}}{\sigma_{\text{P}}^2 + \sigma_{\text{H}}^2} - \frac{1}{\sigma_{\parallel}} \right), \quad (\text{B1})$$

$$\eta_{\text{Ohm}} = \frac{c^2}{4\pi\sigma_{\parallel}}, \quad (\text{B2})$$

$$\eta_{\text{Hall}} = \frac{c^2}{4\pi} \left(\frac{\sigma_{\text{H}}}{\sigma_{\text{P}}^2 + \sigma_{\text{H}}^2} \right); \quad (\text{B3})$$

where the parallel σ_{\parallel} , Pedersen σ_{P} , and Hall σ_{H} conductivities are related to the Hall parameter β_{i,H_2} as:

$$\sigma_{\parallel} = \frac{ecn(\text{H}_2)}{B} \sum_i Z_i x_i \beta_{i,\text{H}_2}, \quad (\text{B4})$$

$$\sigma_{\text{P}} = \frac{ecn(\text{H}_2)}{B} \sum_i \frac{Z_i x_i \beta_{i,\text{H}_2}}{1 + \beta_{i,\text{H}_2}^2}, \quad (\text{B5})$$

$$\sigma_{\text{H}} = \frac{ecn(\text{H}_2)}{B} \sum_i \frac{Z_i x_i}{1 + \beta_{i,\text{H}_2}^2}; \quad (\text{B6})$$

where x_i is the abundance of charged species i with respect to H_2 molecules. The Hall parameter β_{i,H_2} is the key quantity that determines the relative importance of the Lorentz and drag forces for each charged species i in a sea of neutral H_2 molecules. It is defined as:

$$\beta_{i,\text{H}_2} = \left(\frac{Z_i e B}{m_i c} \right) \frac{m_i + \overline{m}_{\text{H}_2}}{\mu m_{\text{H}} n(\text{H}_2) < \sigma \nu >_{i,\text{H}_2}}, \quad (\text{B7})$$

where m_i and $Z_i e$ are the mass and the charge of charged species i , respectively, and $< \sigma \nu >_{i,\text{H}_2}$ is the momentum transfer rate coefficient, parametrized as a function of temperature (Pinto & Galli

2008), which quantifies the collisional coupling between neutral (H_2) and charged (i) species.

APPENDIX C: CHEMICAL ABUNDANCES FOR

$a_{\text{min}} = 0.04 \mu\text{m}$ CASE

Fig. C1 shows the fractional abundances computed using a truncated MRN size distribution with $a_{\text{min}} = 0.04 \mu\text{m}$, which is used for the discussion in § 3.2.

REFERENCES

- Acharyya, K., Hassel, G. E., & Herbst, E. 2011, *ApJ*, 732, 73
 Aikawa, Y., Ohashi, N., Inutsuka, S.-I., Herbst, E., & Takakuwa, S. 2001, *ApJ*, 552, 639
 Aikawa, Y., Herbst, E., Roberts, H., & Caselli, P. 2005, *ApJ*, 620, 330
 Armitage, P. J. 2011, *ARA&A*, 49, 195
 Bai, X.-N., *ApJ*, 739, 50
 Belloche, A., & André, P. 2004, *A&A*, 419, 35
 Bergin, E. A., Alves, J., Huard, T., & Lada, C. J. 2002, *ApJ*, 570, 101
 Bergin, E. A., & Langer, W. D. 1997, *ApJ*, 486, 316
 Bergin, E. A., & Tafalla, M. 2007, *ARA&A*, 45, 339
 Caselli, P., Walmsley, C. M., Zucconi, A., Tafalla, M., Dore, L., & Myers, P. C. 2002, *ApJ*, 565, 331
 Caselli, P., Walmsley, C. M., Zucconi, A., Tafalla, M., Dore, L., & Myers, P. C. 2002, *ApJ*, 565, 344
 Caselli, P., van der Tak, F. F. S., Ceccarelli, C., & Bacmann, A. 2003, *A&A*, 403, 37
 Caselli, P., Bizzocchi, L., Keto, E., Sipilä, O., Tafalla, M., Pagani, L., Kristensen, L. E., van der Tak, F. F. S., Walmsley, C. M., Codella, C., Nisini, B., Aikawa, Y., Faure, A., & van Dishoeck, E. F. 2017, *A&A*, 603, 1
 Cazaux, S., Martín-Doménech, R., Chen, Y. J., Muñoz Caro, G. M., & González Díaz, C. 2017, *ApJ*, 849, 80
 Cecchi-Pestellini, C., & Aiello, S. 1992, *MNRAS*, 258, 125
 Draine, B. T., & Sutin, B. 1987, *ApJ*, 320, 803
 Dzyurkevich, N., Commerçon, B., Lesaffre, P., & Semenov, D. 2017, *A&A*, 603, 105
 Flower, D. R., Pineau des Forêts, G., & Walmsley, C. M. 2005, *A&A*, 436, 933
 Garrod, R. T., Weaver, S. L. W., & Herbst, E. 2008, *ApJ*, 682, 283
 Geppert, W. D., Thomas, R., Semaniak, J., Ehlerding, A., Millar, T. J., Österdahl, F., af Ugglas, M., Djurić, N., Paál, A., & Larsson, M. 2004, *ApJ*, 609, 459
 Hasegawa, T. I., & Herbst, E. 1993, *MNRAS*, 261, 83
 Hirashita, H. 2012, *MNRAS*, 422, 1263
 Ivlev, A. V., Padovani, M., Galli, D., & Caselli, P. 2015, *ApJ*, 812, 135
 Ivlev, A. V., Akimkin, V. V., & Caselli, P. 2016, *ApJ*, 833, 92
 Iqbal, W., & Wakelam, V. 2018, arXiv:1802.07979
 Jørgensen, J. K., Schöier, F. L., & van Dishoeck, E. F. 2004, *A&A*, 416, 603
 Kunz, M., & Mouschovias, T. Ch. 2009, *ApJ*, 693, 1895
 Kunz, M., & Mouschovias, T. Ch. 2010, *ApJ*, 408, 322
 Léger, A., Jura, M., & Omont, A. 1985, *A&A*, 144, 147
 Li, Z.-Y., Krasnopolsky, R., & Shang, H. 2011, *ApJ*, 738, 180
 Marchand, P., Masson, J., Chabrier, G., Hennebelle, P., Commerçon, B., & Vaytet, N. 2016, *A&A*, 592, 18
 Maret, S., Bergin, E. A., & Lada, C. J. 2006, *Nature*, 442, 425
 Mathis, J. S., Rumpl, W., & Nordsieck, K. H. 1977, *ApJ*, 217, 425
 McElroy, D., Walsh, C., Markwick, A. J., Cordiner, M. A., Smith, K., & Millar, T. J. 2013, *A&A*, 550, 36
 Molyarova, T., Akimkin, V., Semenov, D., Henning, T., Vasyunin, A., & Wiebe, D. 2017, *ApJ*, 849, 130
 Nakano, T., Nishi, R., & Umebayashi, T. 2002, *ApJ*, 573, 199
 Harada, N., Hasegawa, Y., Aikawa, Y., Hirashita, H., Liu, H. B., & Hirano, N. 2017, *ApJ*, 837, 78
 Nishi, R., Nakano, T., & Umebayashi, T. 1991, *ApJ*, 368, 181

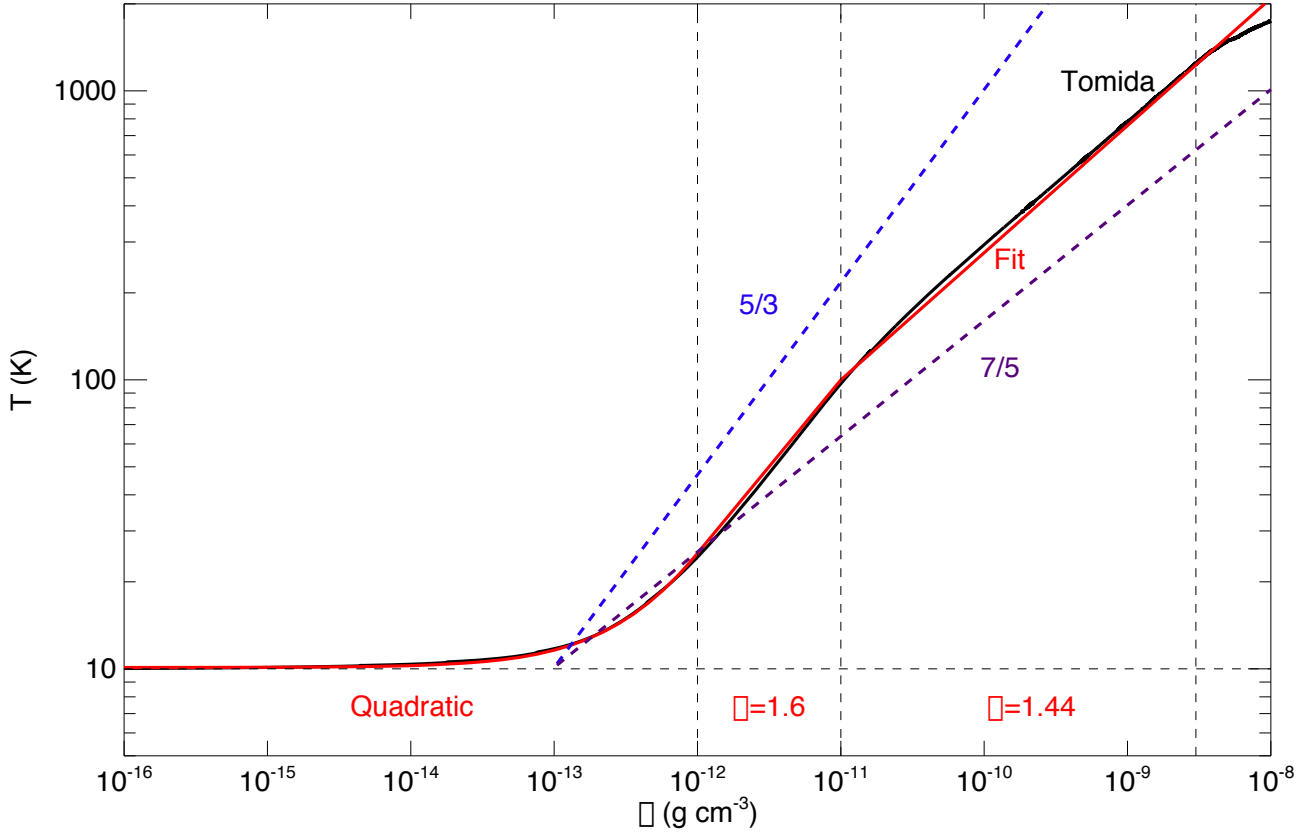


Figure A1. Function fitting (red solid curve) for the evolutionary track from Tomida et al. (2013) (black solid curve). The barotropic EOS with adiabatic indices of 5/3 and 7/5 are shown in blue dashed and purple dashed lines.

Öberg, K. I., van Broekhuizen, F., Fraser, H. J., Bisschop, S. E., van Dishoeck, E. F., & Schlemmer, S. 2005, *ApJ*, 621, 33
 Oppenheimer, M., & Dalgarno, A. 1974, *ApJ*, 192, 29
 Padovani, M., Galli, D., Hennebelle, P., Commerçon, B., & Joos, M. 2014, *A&A*, 571, 33
 Pinto, C., & Galli, D. 2008, *A&A*, 484, 17
 Shen, C. J., Greenberg, J. M., Schutte, W. A., & van Dishoeck, E. F. 2004, *A&A*, 415, 203
 Shimonishi, T., Nakatani, N., Furuya, K., & Hama, T. 2018, arXiv:1801.08716
 Sipilä, O., Caselli, P., & Harju, J. 2015, *A&A*, 578, 55
 Tafalla, M., Myers, P. C., Caselli, P., & Walmsley, C. M. 2004, *A&A*, 416, 191
 Tassis, K., Willacy, K., Yorke, H. W., & Turner, N. J. 2012, *ApJ*, 754, 6
 Tielens, A. G. G. M. 2005, *The Physics and Chemistry of the Interstellar Medium*, Cambridge University Press, ISBN 0521826349
 Tomida, K., Tomisaka, K., Matsumoto, T., Hori, Y., Okuzumi, S., Machida, M. N., & Saigo, K. 2013, *ApJ*, 763, 6
 Umebayashi, T. 1983, *Prog. Theor. Phys.*, 69, 480
 Umebayashi, T., & Nakano, T. 1990, *MNRAS*, 243, 103
 van Dishoeck, E. F., & Blake, G. A. 1998, *ARA&A*, 36, 317
 Wardle, M., & Ng, C. 1999, *MNRAS*, 303, 239
 Wardle, M. 2007, *Ap&SS*, 311, 35
 Wurster, J. 2016, *Publ. Astron. Soc. Australia*, 33, 41
 Zhao, B., Caselli, P., Li, Z.-Y., Krasnopolsky, R., Shang, H., & Nakamura, F. 2016, *MNRAS*, 460, 2050
 Zhao, B., Caselli, P., Li, Z.-Y., & Krasnopolsky, R. 2018, *MNRAS*, 473, 4868

This paper has been typeset from a $\text{\TeX}/\text{\LaTeX}$ file prepared by the author.

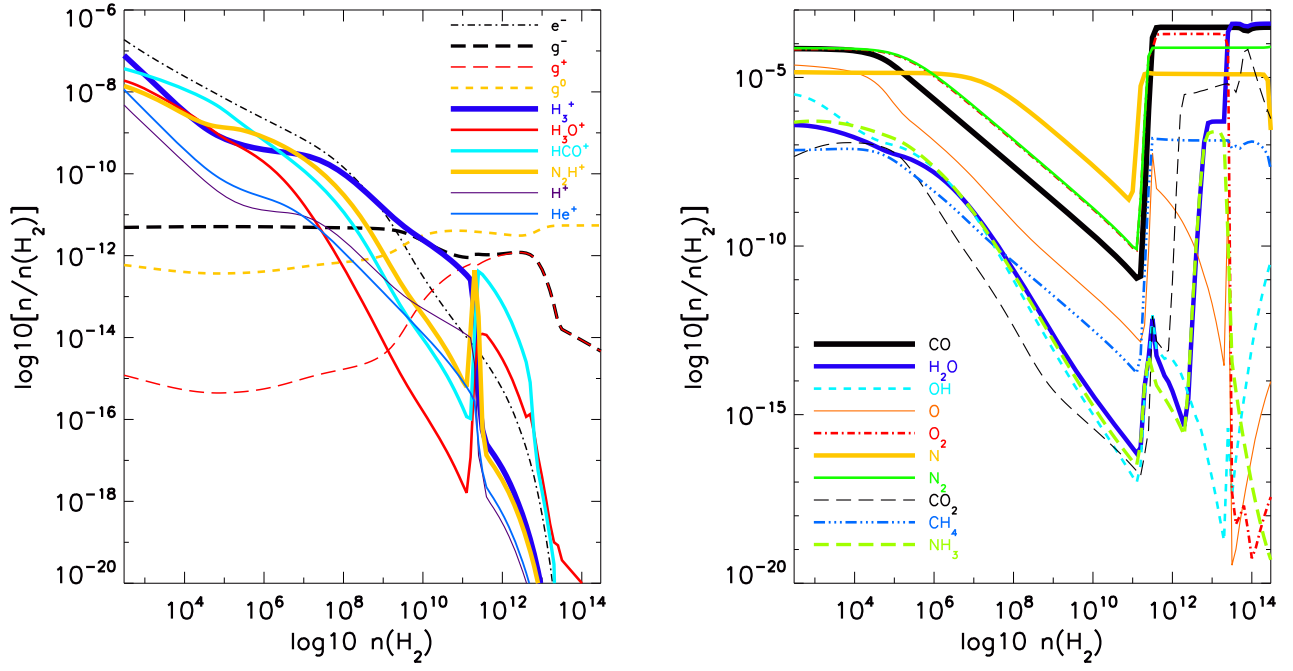


Figure C1. Fractional abundances of the main ion and neutral species computed using the new formulation of cosmic-ray desorption rate for $a_{\min} = 0.04 \mu\text{m}$.